Biology and Chemistry Faculty Publications and Presentations

Department of Biology and Chemistry

11-2023

Ionic partitioning of KCl in AOT reverse micelles from molecular dynamics simulations

Max Crowder

Isabel Lizarraga

Joshua D. Patterson

Arun K. Sharma

Follow this and additional works at: https://digitalcommons.csumb.edu/biochem_fac
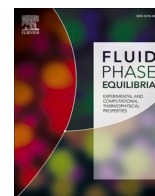
Ionic partitioning of KCl in AOT reverse micelles from molecular dynamics simulations

Max Crowder [a], Isabel Lizarraga [a], Joshua D. Patterson [b], Arun K. Sharma [a,*]

[a] Department of Biology & Chemistry, California State University Monterey Bay, Seaside, CA 93955, United States
[b] Department of Molecular Biology & Chemistry, Christopher Newport University, Newport News, VA, United States

ARTICLE INFO

ABSTRACT

Reverse micelles are an important class of nanoreactors providing an array of applications. The structure and dynamics of aqueous reverse micelles have been intensely investigated, yet there are many subtleties involved in characterizing the arrangement of water and ionic species within these aggregates. The interfacial arrangement of water and dopants added to bis(2-ethylhexyl) sulfosuccinate sodium salt (AOT) reverse micelles were investigated by fully atomistic molecular dynamics simulations. Reverse micelles of increasing water to surfactant ratio were doped with concentrations of KCl from 0.0 to 1.0 M to analyze the partitioning of ions and water. Detailed analysis of pair density functions reveals that Cl^- ions are embedded deep in the aqueous interior, and the K^+ ions display a remarkable affinity for the interface. Our results confirm the existence of multiple layers of water, and an ordered multi-layer ionic arrangement that is driven by the negatively charged surfactant headgroup.

1. Introduction

The unique properties of reverse micelles (RMs) in solution allow them to play essential roles in a broad range of research applications; from simulating cellular membranes for protein dynamics studies, to serving as nanoreactors for nanoparticles synthesis, and functioning as proxies for atmospheric aerosols [1–11]. In particular, the simple preparation and tunable nature of RMs has made them a desirable platform for numerous chemical studies. Synthesis is achieved by stabilizing a polar phase, frequently H_2O, in a surrounding nonpolar phase through the addition of surfactant molecules. The size of RMs can easily be altered by adjusting the molar ratio of H_2O to surfactant, $w_0 = [H_2O]/[surfactant]$.

While the use of RMs has helped reveal many of the unique features of interfacial H_2O, RMs have also proven to be a vital platform for examining ionic properties. Many of the most used surfactants for RM synthesis, bis(2-ethylhexyl) sulfosuccinate sodium salt (AOT), sodium dodecyl sulfate (SDS), and cetyltrimethylammonium bromide (CTAB) are composed of ionic headgroups, $R-SO_3^-$, $R-O-SO_3^-$, and $R-N^+(CH_3)_3$ coupled to counter-ions, such as Na^+ and Br^-. The structural morphology of RMs thus creates an environment that is enriched in ionic species. Numerous studies have sought to further modify the ionic

environment of RMs by changing the counter-ion identity [12–14], by the inclusion of ionic dopants [15,16], or by replacing the polar interior with ionic liquids [17–19]. Indeed, many of the environments that RMs have been employed to simulate, from cellular membranes to atmospheric aerosols, possess a wide variety of ions at varying concentrations, making RMs a viable proxy system.

Unlike in bulk solution, where ions are evenly distributed, ions have been shown to possess inherent affinities toward interfaces. Based on multiple experimental and computational observations interfacial affinity appears to be influenced by both charge identity (cationic vs. anionic) and charge/size ratio [11,16,20–28]. Well-defined interfaces created by the surfactant molecules, the confined nature of the aqueous interior, and the ability to access ionic concentrations beyond those in bulk solution, have made RM structures an appealing system for examining ionic gradients and interfacial affinities.

The distributions and structural arrangements of ions at surfaces and interfaces are often described in terms of paired charge layers referred together as the double layer (DL) or electrical double layer [29]. However, ionic layering can deviate from the double layer structure as the number of ionic species increases. Studies of $NaBr/NaNO_3$ and $NaCl/NaNO_3$ systems observed that Cl^- and Br^- increase the density profile of NO_3^- towards the interface [20,22]. In both systems the maxima of the

---

* Corresponding author.
  E-mail address: arsharma@csumb.edu (A.K. Sharma).

density profiles maintained the order Br^- or $Cl^- < Na^+ < NO_3^-$ in terms of distance from the surface. Increasing the relative concentrations of Br^- and Cl^- to NO_3^- further drew NO_3^- toward the interface, but the anionic species remain separated by a cationic layer of Na^+ in a three-layer system. Hua et al. also proposed a multi-layered ion distribution model based on heterodyne detected vibrational sum frequency generation spectroscopy studies of H_2SO_4 and HSO_4^- salts, in which interfacial-affinity was ordered as $H_3O^+ > HSO_4^- > Na^+$, NH_4^+, $Mg^{2+} > SO_4^{2-}$ [30]. Studies of sea salt aerosols generated with the marine aerosol reference tank noted that treatment with HNO_3 altered the surface ordering of cations from $Ca^{2+} > K^+$ and $Mg^{2+} > Na^+$ pretreatment to $Na^+ > K^+$ and $Mg^{2+} > Ca^{2+}$ post treatment, while anionic order remained relatively unaffected, with the exception of NO_3^- localizing above Cl^- and SO_4^{2-} [31]. Additionally, recent studies have noted the presence of ion-ion interaction pairs in air-water interfaces and electrolyte solutions [25,32,33]. These ionic species not only appear to have their own intrinsic interfacial affinities, outside of the general framework for solvated ions, but also provide the potential to alter the ionic arrangements within the interface.

Experimental and computational approaches have both provided vital information about ionic distributions at interfaces and the properties of RMs. The question of onset of bulk-like water behavior within RMs has attracted significant attention. Multiple studies allude to the identification of multiple layers through analysis of dynamical properties of ions and water molecules with RMs [34–36]. However, investigations into impact of nanoconfinement in AOT reverse micelles of binding interactions between phenosafranin and safranin-O with DNA duplex arrive at the conclusion that even with large reverse micelles (w0-greater than 10), bulk-like behavior is not truly achieved [37,38]. In particular, Molecular Dynamics (MD) simulations of RMs, have played an important role in advancing our understanding of these systems, as MD simulations can capture molecular-scale details that are difficult to access with other methods [12,39–43]. Earlier simulations employed united-atom approaches to model the non-polar hydrocarbon tail of the surfactant [44]. Recent computational advances have moved closer to experimental conditions, simulating self-assembly of a $w_0=5$ RM from first-principles [45]. Here, we use a fully atomistic MD simulation approach to examine the properties of AOT RMs doped with KCl at varying concentrations. Fully atomistic simulations allow for the observation of ionic distributions within the aqueous interior of the RMs as well as structural modifications induced by the presence of ionic dopants. We observed that both size and shape of the RMs are impacted by the addition of KCl. Radial distributions functions (RDFs) reveal that RM aqueous interior is composed of multiple H_2O and ionic layers. RDF analysis also shows that ions within the aqueous interior exist as both ion-ion interaction pairs and solvated ions.

1.1. Computational methodology

This study investigates the layering of ionic species KCl in AOT RMs. The concentration of KCl is varied and tested with different RM sizes to determine the impact and distribution of ionic species in different water to surfactant environments. Fully atomistic MD simulations for the L2 phase of the ternary system composed of AOT and H_2O in isooctane (ISO) were conducted. All simulations were performed using the open source GROMACS molecular dynamics package [46,47]. The initial configuration of the spherical RM in ISO solvent, including placement of ions, was prepared in Packmol [48] using parameters from previous MD studies [41]. Fixing the number of surfactant molecules and varying the water molecules in the RM to arrive at different RM sizes has been demonstrated as a successful approach to investigate properties of RMs [41,42,49]. We follow a similar approach in our simulations and the composition of each RM is displayed in Table 1.

The starting configurations were minimized to 100 kJ/mol/nm. All simulations were carried out in a cubic box of at least 6.5 nm side length. An all-atom potential was adopted for system components. CHARMM27

Table 1
RM MD simulation compositions.

| | n_{KCl} [a] | | | | | n_{H2O} | n_{AOT} |
	0.0 M	0.25 M	0.5 M	0.8 M	1.0 M		
10	0	2	4	6	8	430	43
15	0	3	6	9	12	645	43
20	0	4	8	12	16	860	43

[a] Number of KCl molecules in the RM aqueous interior to achieve the indicated [KCl].

[50] parameters implemented for AOT and ISO and utilized in previous molecular dynamics studies [39,51,52]were applied. The TIP3P [53] model was used to describe water molecules. Simulations and data analysis were carried out on the EXPANSE [54] supercomputer at San Diego Supercomputing center through XSEDE [55] and ACCESS allocations.

Each system was equilibrated to target temperature and pressure respectively before running MD simulations. The NVT stage of equilibration consisted of six stages with temperatures increased from 50 K to 298 K in steps of 50 K. During each stage the simulation was run for 400 ps. Next, the pressure was equilibrated to 1.013 bar and temperature at 298 K in the NPT ensemble. During the NPT equilibration stage, the position restraints on the RM components (and ions, if present) were slowly released. Each stage of NPT equilibration was run for 200 ps, leading to a total NPT equilibration simulation of 1.2 ns. The particle mesh Ewald method [56] implemented in GROMACS was used to calculate the long-range electrostatics in the system. The production MD stage was run for a duration of 300 ns with a timestep of 2 fs. Each simulation was executed from two distinct starting configurations. The calculated properties are in excellent agreement between those two independent simulation trajectories.

2. Results and discussion

2.1. Size

The size of the RM is calculated as the distance between center of mass of each sulfonate head group and the center of mass of the water core, a metric designed to accommodate the dynamics of the system in these fully atomistic simulations. While the fully atomistic approach does create the possibility of a surfactant molecule escaping the RM structure and thus altering the size calculations, care was taken to minimize the potential impact of this possibly by starting form fully formed and equilibrated RMs, conducting long simulation trajectories, and averaging two independent simulation trajectories. The center of mass of each sulfonate head group and the center of mass of the water core distance was averaged for each simulation timestep to report size of reverse micelle for that timestep. This distance is then averaged for each
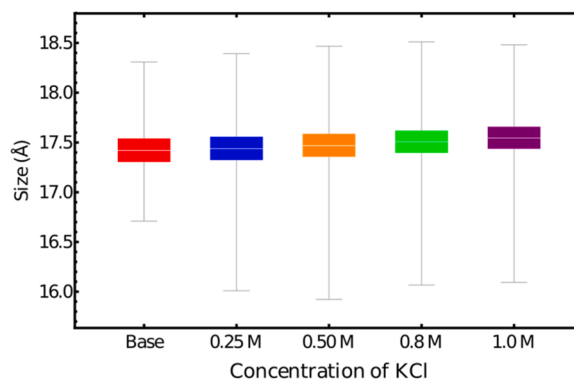
Fig. 1. Size fluctuations for $w_0 = 20$ AOT RMs as a function of KCl doping concentration.

simulation timestep to report size of reverse micelle for that timestep. Fig. 1 displays the size of RMs averaged over two independent simulation runs for $w_0 = 20$ RMs as a function of KCl concentration. At the ionic concentrations investigated in this paper, there does not seem to be a strong impact of concentration of ionic species on the average size of the RMs. However, the variation in size over the course of the simulation does show some sensitivity to KCl concentration. Adding KCl increases the RM sizes observed compared to the base (undoped) case, with the variation in size maximizing at 0.5 M KCl. Beyond 0.5 M, the size variation begins to decrease, but does not converge to the base case conditions. Experimental studies of $w_0 = 10$ AOT RMs doped with NH_4OH, $ZrOCl_2$, and $Al(NO_3)_3$ salts observed both decreases in average RM size as well as narrowing of the associated size distributions with increasing salt concentrations up to 0.6 M at which point the RMs became destabilized [49]. However, with the exception of NH_4OH, the salts used in the study contained highly charged cations, ones that are expected to have low interfacial affinities and necessitate tightly bound solvation shells. Indeed, the authors noted that the critical concentration, at which point RM destabilization was observed, decreased with increasing cationic charge. In contrast, recent studies of $w_0 = 10.5$ AOT RMs noted only modest increases in hydrodynamic diameter with changes in the water-pool composition; increasing from 7.2 nm for the water only case to 7.4 and 7.5 nm for water-pools containing 10% sucrose and 10% sucrose with 1 N HCl, respectively [57]. Similar to our observations, the addition of HCl and/or sucrose, increased the size distribution compared to the undoped case. However, RMs containing both neutral sucrose and ionic HCl showed a narrower distribution in size than the RMs containing sucrose alone.

2.2. Shape

While KCl dopant concentration does not strongly influence average RM size, the potential impact of a dopant on RM structure extends beyond size concerns. Surfactant identity has been known to play a substantial role in shape templating for nanoparticle synthesis, raising important fundamental questions regarding how surfactant-dopant interactions direct overall shape [17,58–60]. By employing fully atomistic simulations, we examine how the addition of an ionic dopant might influence the overall shape of RMs.

RM shape was approximated as ellipsoidal and the three semi-axes, a, b, c, were computed at each time step of the simulations. Eccentricity [43], η, a mathematical expression of shape, for each RM was calculated as,

$$\eta = \sqrt{1 - \frac{c^2}{a^2}}$$

The eccentricity will be zero for a perfectly spherical RM, and increases up to a maximum of 1, for flat or needle like shapes. During the simulation, RMs do not maintain perfectly spherical over the simulation window, but instead fluctuate in shape. Eccentricity values for $w_0 = 20$ RMs were averaged over two independent simulations and plotted as a function of KCl dopant concentration in Fig. 2. Average eccentricity values range from 0.5365 to 0.5195, indicating that the RMs explore multiple shapes over the course of the simulations. Adding KCl decreases the eccentricity, suggesting that the addition of ionic dopants leads to a more spherical average shape. However, adding 1 M KCl only decreases the eccentricity by 3% of the undoped case, implying that this effect is relatively modest. This modest decline in eccentricity in the presence of KCl is replicated in all RM compositions. To further examine the range of shapes explored by the RMs during the simulations, the distributions of eccentricity were calculated for $w_0 = 10$, 15, and 20. Fig. 3 displays the corresponding eccentricity distributions for the undoped RMs, as these conditions resulted in the highest average eccentricities for each w_0. Eccentricity values range from 0.1 to 0.9, indicating a broad range of shapes accessed by the RM structures. Average eccentricity decreases as
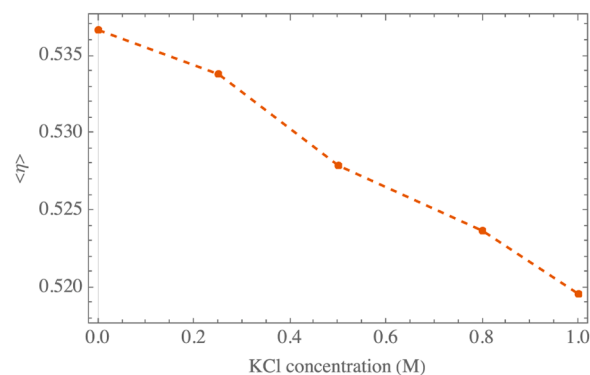
Fig. 2. Shape as measured by eccentricity for $w_0 = 20$ AOT RMs as a function of KCl doping concentration.
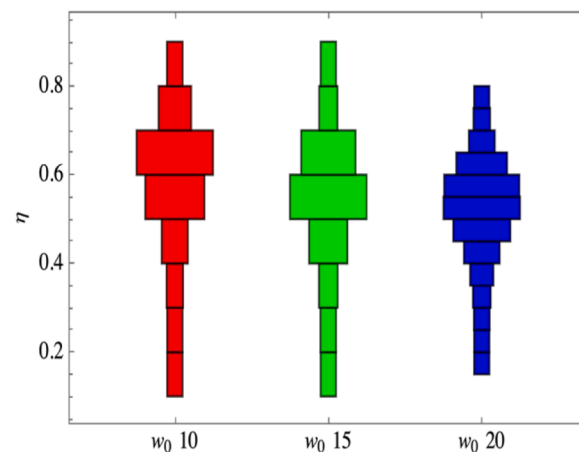
Fig. 3. Distribution chart highlighting the sampling of shapes during the simulation without KCl addition.

w_0 increases. The distribution of eccentricities also decreases with increasing w_0, with $w_0 = 20$ showing a much narrower distribution than $w_0 = 10$ and 15.

2.3. Density profiles

The normalized density profiles of Na^+, K^+, Cl^-, $R-SO_3^-$, and H_2O of a KCl doped $w_0 = 20$ AOT RM are displayed in Fig. 4. The normalized values are obtained by scaling the density value of each species by division with the maximum value for that species. This ensures that the density of each species is in the 0.0 to 1.0 range and all features would be visible on the plot. The density is plotted along a cross-section of the 3-dimensional simulation box. The simulation results support the importance of ion layering in the structural arrangement of the interfacial region. The sulfonate headgroup, represented by $R-SO_3$ has the broadest density profile, consistent with formation of the outer boundary of the RM interfacial region. K^+ is nearly evenly distributed with Na^+, the counter-ion of the $R-SO_3^-$ AOT head group, suggesting that K^+ is located along with Na^+ in the interfacial region.

While the cations, K^+ and Na^+ reside together in the interfacial region, Cl^- has a much narrower distribution, suggesting anionic Cl^- is located beneath the cations and away from the interface. The simulation points to a multi-layer model organized in the order: (Interface) $R-SO_3^- > K^+$ and $Na^+ > Cl^-$ (Core). Similar density profiles are observed for all concentrations and w_0 values in our simulations. This clearly indicates that while the arrangement of ionic layering is independent of the amount of added salt, the number of layers formed is dependent on salt identity.
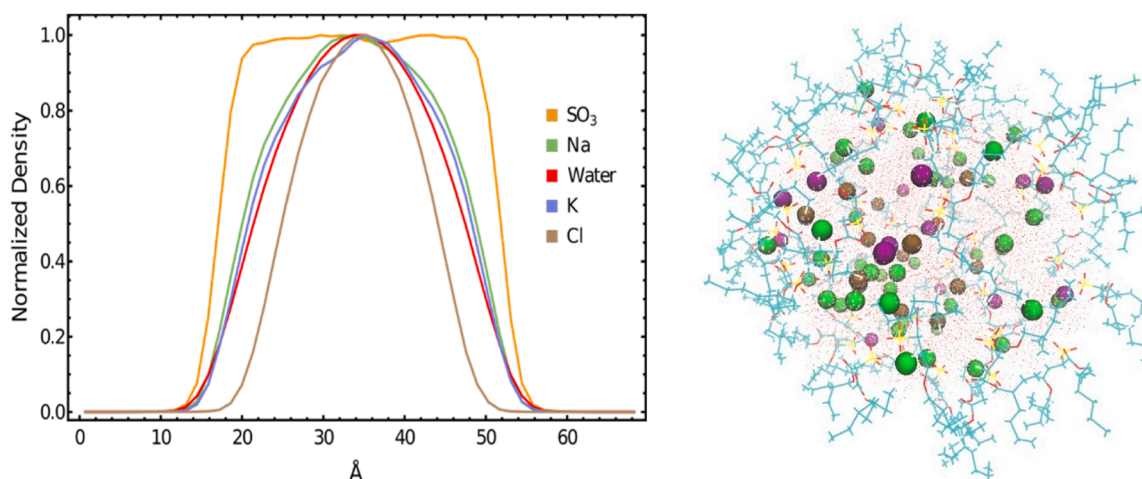
Fig. 4. Normalized density profiles for SO_3^- (orange line), Na^+ (green line), H_2O (red line), K^+ (purple line), and Cl^- (brown line) within a $w_0 = 20$ AOT RM doped with 1.0 M KCl. The distance on the X-axis is the simulation box length. On the right, a snapshot of the reverse micelle is shown without the isooctane solvent. The water molecules are represented by red dots, sodium ions by green beads, potassium ions by purple beads and chloride ions with brown beads.

2.4. Radial density functions

2.4.1. H_2O

RMs have become a model system for examining the unique properties of H_2O in confined environments. Numerous experimental studies seeking to examine the properties of confined H_2O have observed that the aqueous interior of RMs deviate substantially from bulk water characteristics. Frequently, these studies have interpreted their observations in terms of a "shell-core" or "interfacial-core" model in which two distinct H_2O species occupy the aqueous interior. Interfacial waters, those H_2Os interacting with the surrounding surfactant headgroups, are characterized as having distinct vibrational spectra, slower vibrational relaxation rates and reorientation dynamics relative to the core waters, which exhibit bulk-like behavior.

MD simulations have offered a powerful complement to these experimental studies, supporting the presence of multiple H_2O species within the RM interior, and providing new insights regarding the dynamic environment of the aqueous interior. While some studies have adopted the interfacial-core model [12], others have further divided the aqueous interior using a "trapped", "bound", and "free" H_2O model [61]. In this framework, "trapped" waters are defined as those waters multiply coordinated to the SO_3^- headgroups at the interface, while the "free" waters represent those waters that exhibit bulk-like properties. "Bound" waters possess intermediate properties, in terms of both interactions with the surface ions and mobility, between the "trapped" and "free" H_2O classes. These studies used minima within the O atom radial density profiles to distinguish between the three H_2O species.

Here we examine partitioning of H_2O based on the H_2O-SO_3^- radial density function (RDF). The H_2O-SO_3^- pair density profile for a $w_0 = 20$ undoped RM is displayed in Fig. 5. The profile shows a sharp peak at 1.80 Å followed by a deep minimum located at 2.38 Å. The profile then increases rapidly to reveal a series of peaks at 3.12, 4.06, 5.04, and 6.40 Å before tailing after a shallow minimum at 8.74 Å. The observation of multiple peaks suggests that several well-defined layers of H_2O exist within the aqueous interior.

To examine the partitioning between individual H_2O layers, the radial density profiles were integrated based on areas between identified minima. The fractional populations in each layer for the $w_0 = 20$ RMs are displayed in Table 2. Table S1 and Table S2 present the corresponding data for the $w_0 = 10$ and $w_0 = 15$ RMs, respectively. In general, the fractional population increases with each subsequent layer and is dominated by the sixth layer, which contains over half of all the waters within the aqueous interior. Previous studies of $w_0 = 10$ AOT RMs noted fractional populations of 0.19, 0.26, and 0.55 for the trapped, bound,
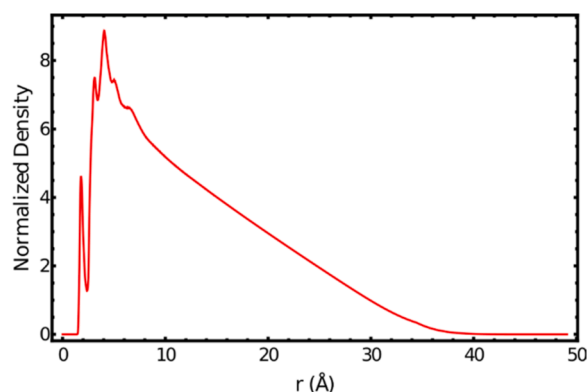
Fig. 5. Normalized SO_3^- H_2O radial density function within a $w_0 = 20$ AOT RM without any added KCl.

Table 2
Fractional H_2O layer populations upon KCl addition.

$w_0 = 20$					
H_2O Layer (Ranges, Å)	[KCl] M				
	0.0	0.25	0.5	0.8	1.0
Layer 1 (0.00–2.38 Å)	0.0194	0.0198	0.0193	0.0193	0.0193
Layer 2 (2.38–3.42 Å)	0.0494	0.495	0.0496	0.0496	0.0484
Layer 3 (3.42–4.81 Å)	0.0969	0.0951	0.0962	0.0987	0.0986
Layer 4 (4.81–5.80 Å)	0.0601	0.0655	0.0615	0.0576	0.0647
Layer 5 (5.80–8.74 Å)	0.161	0.159	0.161	0.162	0.156
Layer 6 (>8.74 Å)	0.614	0.611	0.612	0.613	0.613

and free H_2O classifications [61,62]. Combining the observed fractional populations for layers 1, 2, and 3 within the $w_0 = 10$ undoped RM, results in a population of 0.196, while combining layers 4 and 5, yields a population of 0.251. Taken together with layer 6′s fractional population of 0.553, we see excellent agreement with these previous studies.

As w_0 is increased the fractional populations shift, with layers 1–5 decreasing and layer 6 rapidly increasing. Studies employing an interfacial-core model have previously noted that the fractional population of interfacial H_2O is expected to decrease with increasing w_0, while the fraction of core H_2O is expected to increase [63–66]. Based on these distinctions, layers 1–5 would be described as interfacial H_2O and account for as much as 0.386 of all H_2O in the RM, while layer 6 would be described as core H_2O. Similarly, Faeder and Ladanyi observed that

both the trapped and bound H_2O classifications decreased in fractional population as RM size increased from $w_0 = 1$ to $w_0 = 10$, while the free H_2O population increased in fraction [61,62]. While our studies observe similar trends, individual layer analysis reveals that while layers 1–5 all decrease with increasing RM size, individual layers change fractional populations at different rates. Layer 1, consisting of the waters located closest to the SO_3^- headgroups, shows a very modest response to w_0, decreasing from 0.0204 at $w_0 = 10$ to 0.0194 at $w_0 = 20$; corresponding to a relative reduction of 5% within the layer. Layer 3 shows the greatest sensitivity to changes of w_0, undergoing a 16% reduction in fraction from $w_0 = 10$ to 20. Although these observations are based on a relatively narrow range of w_0 ratios, the response of individual layers to changes of w_0 raises interesting questions regarding the organization of H_2O within the RM interior and we are actively working to extend our studies to more w_0 ratios.

While the partitioning of H_2O between individual layers is sensitive to changes in w_0 ratio, the allocation of H_2O does not appear to be influenced by the addition of KCl within the aqueous interior. For fixed w_0 sizes the fractional populations in each layer remain consistent between the undoped case and the 1.0 M KCl doped case. Previous studies examining the properties of Na^+, K^+, and Cs^+ AOT RMs, observed that the first peaks in the radial density profiles of H_2O oxygen atoms decreased as the size of the AOT counter-ion was increased, while the first peaks in the counter-ion profiles increased in density as the counter-ion size increased [61]. These observations suggested that the larger K^+ and Cs^+ counter-ions displaced more H_2O within the interfacial region compared to Na^+. Despite the inclusion of K^+ within the aqueous interior, we do not see any indications of H_2O displacement from any of the H_2O layers. However, the cationic profile within the aqueous interior is dominated by the Na^+ counter-ions in our studies, even at the highest KCl doping concentrations. The lack of H_2O response to KCl inclusion suggests that the organization of waters within the aqueous interior may be driven by the need to solvate the SO_3^- headgroups and the corresponding Na^+ counter-ions, rather than by the relative interfacial affinities of Na^+, K^+, and Cl^-.

2.5. Na^+ and K^+

Much like H_2O, several studies have sought to examine the distribution of the AOT counter ions within the aqueous interior. These studies observed that larger counter-ions allocate towards the interface in greater number than smaller counter-ions [61]. Fig. 6 displays the pair density profiles of Na^+ and K^+ relative to the SO_3^- headgroups of $w_0 = 20$ AOT RMs doped with 1.0 M KCl. Both profiles exhibit similar trends: intense first peaks located at short distances, 2.26 and 2.64 Å respectively, followed by deep minimums at 3.07 and 3.37 Å respectively, separating the first and second peaks. These trends are markedly similar to those previously reported for AOT counter-ion density profiles
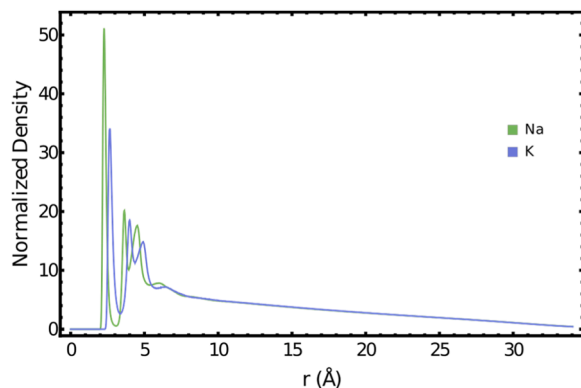
[61,62]. Following the deep minimum, the Na^+ profile exhibits peaks at 3.64, 4.51, and 6.02 Å, while K^+ peaks are located at 4.00, 4.90, and 6.40 Å. The locations of the peaks appear insensitive to both w_0 and KCl doping concentration, suggesting ion identity may play a strong role in dictating location throughout the aqueous interior.

As with H_2O, we examined the partitioning of Na^+ and K^+ between each layer within the aqueous interior. The fractional populations in each ionic layer as a function of KCl concentration for the $w_0 = 20$ RMs are displayed in Table 3. Table S3 and Table S4 present the corresponding data for the $w_0 = 10$ and $w_0 = 15$ RMs, respectively. In the absence of KCl, over half of the Na^+ ions are located within the innermost fifth layer. The next most populated layer is the first layer located closest to the SO_3^- headgroups at the interface, followed by the third and fourth layers. Layer 2 consistently contains the smallest fraction of the Na^+s within the aqueous interior. As w_0 is increased layers 1–3 all decrease in fractional population, with layer 1 showing the greatest sensitivity to w_0 amongst the first 3 layers. Layers 4–5 increase in fractional population as w_0 increases. However, the increase in layer 4 population is very small relative to the increase in layer 5 population. The decrease in the upper layers and corresponding increase in the lower layers with increasing w_0 is consistent with the capacity of the larger aqueous cavity to solvate more ions. K^+ shows a similar response to w_0, decreasing in fractional population in layers 1–3 and increasing in layer 5. Layer 4 is relatively unchanged by w_0 size. Following similar conventions to the treatment of H_2O within RMs, we classify layers 1–3 for both Na^+ and K^+ as interfacial based on decreasing fractional populations with increasing w_0 and account for 0.310 and 0.316 of the fractional populations, respectively. In turn, ions contained within layers 4–5 are classified as core ions.

The addition of KCl causes decreases in the fractional populations of Na^+ within the first 3 layers, with layer 1 showing the largest response to the KCl dopant. Similar to the behavior observed upon changes in w_0, layers 4–5 increase in fractional population of Na^+ as KCl concentration increases. These observations suggest that the addition of K^+ may dislodge some of the Na^+ within the layers closest to the SO_3^- headgroups. To further explore the potential of K^+ to displace Na^+ within the interfacial region, we examined the individual Na^+ and K^+ counts over the course of the simulation within each ionic layer. Ion counts as a function of KCl doping concentration and RM size are displayed in Table 4. Na^+ ion counts in layers 1–3 steadily decreases with increasing KCl concentration while the number of K^+ ions increase, indicating that K^+ is indeed displacing Na^+ within outermost layers of the aqueous interior. However, even at the highest doping concentrations Na^+ remains the dominant cationic species within these layers. While the larger K^+ is expected to have a greater interfacial affinity than Na^+, the differences in relative interfacial affinity may not be great enough to completely displace Na^+ from the interfacial layers in favor of K^+ [20]. Indeed, at 1.0 M KCl 1 Na^+ has been removed from layers 1–3 compared

Fig. 6. Normalized SO_3^-- Na^+ (green line) and SO_3^-- K^+ (purple line) radial density functions within a $w_0 = 20$ AOT RM doped with 1.0 M KCl.

Table 3
Fractional Na^+ and K^+ layer populations upon KCl addition.

$w_0 = 20$					
Na^+ Layer (Ranges, Å)	[KCl] M				
	0.0	0.25	0.5	0.8	1.0
Layer 1 (0.00–3.07 Å)	0.137	0.129	0.126	0.121	0.115
Layer 2 (3.07–3.94 Å)	0.0716	0.0683	0.0663	0.0641	0.0617
Layer 3 (3.94–5.36 Å)	0.147	0.144	0.141	0.137	0.134
Layer 4 (5.36–7.80 Å)	0.132	0.134	0.132	0.131	0.132
Layer 5 (>7.80 Å)	0.512	0.525	0.535	0.547	0.558
K^+ Layer (Ranges, Å)	[KCl] M				
		0.25	0.5	0.8	1.0
Layer 1 (0.00–3.37 Å)		0.121	0.114	0.110	0.106
Layer 2 (3.37–4.36 Å)		0.0911	0.0879	0.0849	0.0825
Layer 3 (4.36–5.84 Å)		0.142	0.134	0.134	0.128
Layer 4 (5.84–8.20 Å)		0.124	0.126	0.121	0.122
Layer 5 (>8.20 Å)		0.522	0.539	0.550	0.561

Table 4

Layer ion counts interaction pairs fractional population.

$w_0 = 20$ Na$^+$ Layer	[KCl] M				
	0.0	0.25	0.5	0.8	1.0
1	5.89	5.55	5.42	5.20	4.95
2	3.08	2.94	2.85	2.75	2.65
3	6.32	6.19	6.06	5.89	5.76
4	5.68	5.76	5.68	5.63	5.68
5	22.0	22.6	23.0	23.5	24.0
K$^+$ Layer	[KCl] M				
		0.25	0.5	0.8	1.0
1		0.482	0.908	1.32	1.70
2		0.364	0.703	1.02	1.32
3		0.568	1.07	1.61	2.05
4		0.496	1.01	1.45	1.95
5		2.09	4.31	6.60	8.98
Cl$^-$ Layer	[KCl] M				
		0.25	0.5	0.8	1.0
1		0.0314	0.0576	0.117	0.137
2		0.140	0.305	0.506	0.666
3		0.191	0.422	0.667	0.803
4		0.238	0.468	0.734	1.17
5		3.40	6.75	9.97	13.2

Table 5

Cl$^-$ layer populations upon KCl addition.

$w_0 = 20$ Cl$^-$ Layer (Ranges, Å)	[KCl] M			
	0.25	0.5	0.8	1.0
Layer 1 (0.00–3.87 Å)	0.00785	0.0072	0.00975	0.00855
Layer 2 (3.87–5.27 Å)	0.0350	0.0381	0.0422	0.0416
Layer 3 (5.27–6.56 Å)	0.0478	0.0527	0.0556	0.0502
Layer 4 (6.56–7.81 Å)	0.0594	0.0585	0.0612	0.0732
Layer 5 (>7.81 Å)	0.850	0.844	0.831	0.827

(interfacial, 0.174 total fraction), while layer 5 (core) increases. As the extent of "bulk-like" core H$_2$O within the aqueous interior increases with increasing w_0, the response of Cl$^-$ to increasing w_0 indicates that Cl$^-$ is excluded from the interfacial region and preferentially allocated within the core; counter to observed Cl$^-$ distributions for air-water interfaces [25,67]. As KCl concentration is increased for a fixed w_0 size the fractional populations in layers 1–4 increase while the population in layer 5 decreases. However, the populations in the first four layers remain extremely modest, never exceeding a total count of 3 Cl$^-$ ions at the highest KCl doping concentrations. The allocation of more Cl$^-$ ions to layers 1–4 as KCl concentration increases may provide a means of balancing some of the charge from the Na$^+$ and K$^+$ within the aqueous interior. Alternatively, Cl$^-$ could transition to the upper layers of the RM once an accommodation limit is reached within the core region of the aqueous interior.

to the 0.0 M KCl case, while 5 K$^+$ ions have been incorporated into the outer layers. The inequivalent exchange of these monovalent ions suggests that other properties, such as charge density and/or Coulombic interactions with the SO$_3^-$ headgroups or Cl$^-$, may be driving the incorporation of K$^+$ into the interfacial region of the RM.

2.6. Cl$^-$

Considerable work has been devoted towards understanding the properties of Cl$^-$ ions in interfacial systems. Numerous experimental and computational studies have observed that Cl$^-$ has a fairly strong interfacial affinity; preferentially allocating closer to the interface than its corresponding counter-ion for air-water interfaces [25]. While these previous studies would suggest that Cl$^-$ should reside closer to the interface than both Na$^+$ and K$^+$ in our simulations, the anionic profile of the interface created by the SO$_3^-$ headgroups of AOT appears to strongly influence the distribution of Cl$^-$ throughout the RM. Much like H$_2$O, Na$^+$, and K$^+$, Cl$^-$ is allocated into a series of layers within the aqueous interior. The Cl$^-$ - SO$_3^-$ pair density profile for a $w_0 = 20$ RM doped with 1.0 M KCl is displayed in Fig. 7. The profile shows a series of peaks at 3.74, 4.86, 6.32, 7.02, and 11.94 Å. The fractional populations of each layer are displayed in Table 5. The majority of the Cl$^-$ ions, 0.827, reside in the innermost layer, with only 0.00855 located within the first layer. As w_0 is increased the fractional populations decrease in layers 1–4

2.7. Ion-ion interactions

The tightly spaced ionic layering pattern observed for Na$^+$, K$^+$, and Cl$^-$ within the RM interior provides the potential for ion-ion interactions. Indeed, several studies have noted the presence of contact pairs (CPs) and solvent-shared ion pairs (SIPs) at air-water interfaces and in electrolyte solutions [25,32,33]. The Na$^+$- Cl$^-$ and K$^+$- Cl$^-$ pair density profiles for a $w_0 = 20$ RM doped with 1.0 M KCl are displayed in Fig. 8. The Na$^+$- Cl$^-$ profile shows distinct peaks at 2.60, 5.00, and 7.18 Å before tailing at longer distances. The radial cutoff for Cl$^-$ has previously been reported as 3.86 Å [25]. The radial cutoff of 3.49 Å suggests the presence of Na$^+$ within the Cl$^-$ solvation shell as a CP. The subsequent peaks at 5.00 and 7.18 Å are indicative of SIPs and are consistent with observed SIP ion distances for Mg^{2+}- Cl$^-$ and Cs$^+$- Cl$^-$. K$^+$- Cl$^-$ profiles show similar results, with peaks at 3.02 (CP), 5.30 (SIP$_1$), and 7.52 Å (SIP$_2$) [32]. The fractional populations of each ion pair are displayed in Table 6. For both Na$^+$ and K$^+$, free solvated ions (FR) represent the most abundant species. However, taken together, most of the Na$^+$ and K$^+$ within the aqueous interior exist in some form of ion-ion interaction species. CPs represent the most common ion-ion interaction species for both Na$^+$ and K$^+$. While a larger fraction of K$^+$ form CPs with

Fig. 7. Normalized SO$_3^-$- Cl$^-$ radial density function within a $w_0 = 20$ AOT RM doped with 1.0 M KCl.
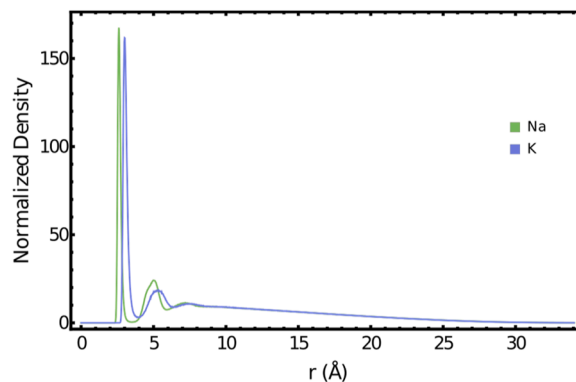
Fig. 8. Normalized Na$^+$ - Cl$^-$ (green line) and K$^+$ - Cl$^-$ (purple line) radial density functions within a $w_0 = 20$ AOT RM doped with 1.0 M KCl.

Table 6
Ion-ion interaction pairs fractional population.

$w_0 = 20$ Na$^+$-Cl$^-$	Cutoff (Å)	[KCl]			
		0.25	0.5	0.8	1.0
CP	3.49	0.187	0.200	0.216	0.230
SIP$_1$	5.92	0.154	0.158	0.155	0.152
SIP$_2$	8.51	0.134	0.130	0.137	0.135
FR		0.526	0.512	0.492	0.483
K$^+$-Cl$^-$	Cutoff (Å)	[KCl]			
		0.25	0.5	0.8	1.0
CP	3.92	0.250	0.261	0.270	0.282
SIP$_1$	6.42	0.155	0.151	0.153	0.147
SIP$_2$	9.03	0.127	0.132	0.130	0.136
FR		0.469	0.456	0.447	0.436

Cl$^-$ than Na$^+$, this may be an artifact of the substantially lower concentration of K^+ relative to Na$^+$ within the aqueous interior. Increasing the KCl concentration increases the fractional populations of both the K^+- Cl$^-$ and Na$^+$- Cl$^-$ CPs while decreasing the population of fully solvated ions. Interestingly, neither of the SIP populations show a response to increasing KCl concentration. The shorter separation species, SIP$_1$, possesses a higher fractional population for both the K^+- Cl$^-$ and Na$^+$- Cl$^-$ interaction pairs than the more separated SIP$_2$ species. In addition, both K^+- Cl$^-$ and Na$^+$- Cl$^-$ interaction pair species have similar fractional populations, ~0.15 and ~0.13 for the SIP$_1$ and SIP$_2$ species, respectively. Previous studies have noted increases in SIP population with increasing electrolyte concentration in bulk-solution. As such, the insensitivity of the K^+- Cl$^-$ and Na$^+$- Cl$^-$ SIP populations to KCl concentration suggests that formation of SIPs in this case may be driven by the overall ionic structure within the aqueous interior rather than KCl concentration.

2.8. RM ionic structure

By examining the distributions of each component of the RM aqueous interior, we were able to develop a framework for how ions are dispersed throughout this complex environment. When examined together the ion RDFs reach maxima in the same regions where the H$_2$O RDFs are in minima, indicating that RM aqueous interior is composed of an ordered and layered structure of altering ionic layers separated by aqueous layers. The SO$_3^-$ headgroups interact directly with the first aqueous layer, which accounts for only a small fraction of the interior waters, 0.0193. However, this small number of waters is not enough to balance the charge density at the interface. In response, the first Na$^+$ and K^+ layers act as CPs with the SO$_3^-$ headgroups to further balance the negative charge to the interface. As K^+ concentration is increased within the RM interior, some of the Na$^+$ ions are displaced from the first layer in favor of K^+ ions. However, the first ionic layer remains dominated by the more abundant and more densely charged Na$^+$ ions. Anionic Cl$^-$ is completely excluded from the first ionic layer due to electrostatic repulsion with the SO$_3^-$ headgroups. A second aqueous layer, peaking near 3.12 Å and extending to a radial cutoff of 3.42 Å, follows the first ionic layer. These distances are within previously observed solvation shell radial cutoffs for Mg^{2+}, Cl$^-$, and SO$_4^{2-}$ at 3.00, 3.86, and 4.64 Å [25, 32], respectively. As such, the second aqueous layer likely functions as both a solvation layer and the solvent within SIPs between the SO$_3^-$ headgroups and Na$^+$ and K^+ ions in the second ionic layer below. Na$^+$ and K^+ populate the second ionic layer. RDF peaks at 3.64 and 4.00 Å, for the Na$^+$- SO$_3^-$ and K^+- SO$_3^-$ ion pair profiles respectively, support the presence of SIPs within this second ionic layer. The second ionic layer is nearly devoid of Cl$^-$, with a fractional population of <0.0219. The nonzero fractional population is likely due to a Cl$^-$ ion located near the interface at early times in the simulation prior to diffusing to deeper ionic layers within the RM interior. The third aqueous layer peaks at 4.04 Å and corresponds to the largest density within the H$_2$O RDF. This

layer likely represents the first aqueous layer outside of the SO$_3^-$ solvation shell. Indeed, the sensitivity of the third aqueous layer to changes in w_0 supports the assignment of this layer as a more labile form of H$_2$O compared to the first two aqueous layers. The third aqueous layer gives way to another ionic layer. The Na$^+$ and K^+ RDF peaks begin to broaden, suggesting a larger distribution of distances from the SO$_3^-$ headgroups. Na$^+$ is localized closer to the RM interface than K^+ in the third ionic layer, while K^+ and Cl$^-$ maximize at the same distance, ~4.92 Å. However, the Cl$^-$ RDF spans both the Na$^+$ and K^+ layers, indicating that while modest in abundance, the Cl$^-$ located within this layer is localized with the Na$^+$ and K^+ ions. This observation supports the presence CPs between the Na$^+$ and K^+ ions with Cl$^-$ in the third ionic layer. Following the third aqueous and ionic layers the H$_2$O, Na$^+$, and K^+ RDFs decrease substantially in density and the peaks broaden, while the Cl$^-$ RDF continues to increase. The increased presence of Cl$^-$ provides the potential for further CP formation as well as SIP formation with Na$^+$ and K^+ located within the upper and lower ion layers. The layering pattern continues for another two aqueous and ionic layers before the identification of peaks within the H$_2$O, Na$^+$, and K^+ RDFs becomes unclear as the peaks are superimposed on top of a gradual decay at longer distances. The Cl$^-$ RDF continues to reveal additional peaks, suggesting that there may be more layers deeper in the aqueous interior. However, the increase in breadth of the RDF peaks, particularly for H$_2$O, indicates a transition to bulk-like properties somewhere in the region of the fourth or fifth layers, consistent with interfacial-core distinctions, as the broader RDF peaks imply a greater extent of species mobility and greater separation between individual ions.

3. Conclusions

Interfacial-core distinctions have been consistently utilized to explain the dynamics, structural properties, and partitioning of H$_2$O and ionic species within the interior of RMs. This approach has proven quite successful and has been a crucial approach for revealing the unique properties of the interfacial region. By examining the impact of a KCl dopant on the properties of the RMs over a variety of w_0 ratio we can further highlight the complex nature of the interfacial region. Rather than being composed of a single species, distinct from their core counterparts, the interfacial region is populated by a host of chemical species. In our studies, as many as 5 H$_2$O layers can be classified as interfacial; representing not only those H$_2$Os in direct contact with the SO$_3^-$ headgroups, but also H$_2$Os solvating the surfactant counter-ions and H$_2$Os and those incorporated into SIPs. Given the diversity of species contained within the H$_2$O layers of the interfacial region, it is perhaps unsurprising that these layers exhibit different responses to increasing w_0. Sophisticated time-resolved 2D-IR spectroscopy has also proposed the layer-wise structure of water molecules in these reverse micelles. These experimental results [68,69] provide strong validation and support for our computational analysis. The diversity of ionic species within the interfacial region appears to be equally rich, containing CPs, SIPs, as well as solvated ions. Na$^+$ and K^+ co-localize within discrete layers through the interfacial and core regions of the RM aqueous interior. While Na$^+$ is the dominant cationic species within the observed interfacial layers, increasing additions of KCl lead to small displacements of Na$^+$ in favor of K^+. Cl$^-$ is almost completely excluded from the outermost ionic layers and is predominately observed within the core region. While Cl$^-$ has been observed to have a stronger relative interfacial affinity than Na$^+$ and K^+ in air-water interfaces [27,28,25], the need to maintain charge layering within the aqueous interior of the RMs seems to be a strong driver of the distribution of ionic species and appears to outweigh intrinsic interfacial affinities. The highly charged nature of the aqueous interior places a strong priority on balancing Coulombic interactions. The observed lack of response of size and dynamic sampling of shapes even with the addition of KCl highlights the role charge interactions play in the overall structure of aqueous interior.

Supporting information

Fractional Layer Populations for H_2O, (Tables S1 and S2), Na^+ and K^+(Tables S3 and S4), and Cl^- (Tables S5 and S6) for $w_0 = 10$ and 15 AOT RMs, respectively. (PDF)

Author contributions

The manuscript was written through contributions of all authors. All authors have given approval to the final version of the manuscript. ‡†These authors contributed equally.

Funding sources

CRediT authorship contribution statement

Max Crowder: Data curation, Writing – original draft, Investigation. **Isabel Lizarraga:** Data curation, Formal analysis, Investigation. **Joshua D. Patterson:** Investigation, Writing – review & editing, Validation, Visualization, Funding acquisition, Writing – original draft, Conceptualization, Methodology, Project administration. **Arun K. Sharma:** Supervision, Project administration, Funding acquisition, Writing – original draft, Writing – review & editing, Conceptualization, Methodology, Software.

Declaration of Competing Interest

There are no competing interests.

Data availability

Data will be made available on request.

Acknowledgement

Supplementary materials

Supplementary material associated with this article can be found, in the online version, at doi:10.1016/j.fluid.2023.113904.

References

[1] N.E. Levinger, L.C. Rubenstrunk, B. Baruah, D.C. Crans, Acidification of reverse micellar nanodroplets by atmospheric pressure CO_2, J. Am. Chem. Soc. 133 (2011) 7205–7214, https://doi.org/10.1021/ja2011737.

[2] J.A. Gutierrez, J. Cruz, P. Rondón, N. Jones, C. Ortiz, Small gold nanocomposites obtained in reverse micelles as nanoreactors. Effect of surfactant, optical properties and activity against Pseudomonas aeruginosa, New J. Chem. 40 (2016) 10432–10439, https://doi.org/10.1039/c6nj02259f.

[3] J.A. Gutiérrez, S. Caballero, L.A. Díaz, M.A. Guerrero, J. Ruiz, C.C. Ortiz, High antifungal activity against candida species of monometallic and bimetallic nanoparticles synthesized in nanoreactors, ACS Biomater. Sci. Eng. 4 (2018) 647–653, https://doi.org/10.1021/acsbiomaterials.7b00511.

[4] R. Saha, S. Rakshit, P.K. Verma, R.K. Mitra, S.K. Pal, Protein-cofactor binding and ultrafast electron transfer in riboflavin binding protein under the spatial confinement of nanoscopic reverse micelles, J. Mol. Recognit. 26 (2013) 59–66, https://doi.org/10.1002/jmr.2246.

[5] L.K. Shrestha, R.G. Shrestha, N. Vilanova, C. Rodriguez-Abreu, K. Ariga, *In-situ* formation of silver nanoparticles using nonionic surfactant reverse micelles as nanoreactors, J. Nanosci. Nanotechnol. 14 (2014) 2238–2244, https://doi.org/10.1166/jnn.2014.8548.

[6] L. Qi, J. Ma, H. Cheng, Z. Zhao, Reverse micelle based formation of $BaCO_3$ nanowires, J. Phys. Chem. B 101 (1997) 3460–3463, https://doi.org/10.1021/jp970419k.

[7] H. Shi, L. Qi, J. Ma, H. Cheng, Synthesis of single crystal BaWO4 nanowires in catanionic reverse micelles, Chem. Commun. (2002) 1704–1705, https://doi.org/10.1039/b204995c.

[8] M.P. Pileni, Reverse micelles as microreactors, J. Phys. Chem. 97 (1993) 6961–6973, https://doi.org/10.1021/j100129a008.

[9] J.Y. Lee, J. Lee, Y.J. Jang, J. Lee, Y.H. Jang, S.T. Kochuveedu, S.S. Lee, D.H. Kim, Plasmonic nano-necklace arrays via reconstruction of diblock copolymer inverse micelle nanotemplates, Soft Matter 7 (2011) 57–60, https://doi.org/10.1039/C0SM00972E.

[10] S. Xu, H. Zhou, J. Xu, Y. Li, Synthesis of size-tunable silver iodide nanowires in reverse micelles, Langmuir 18 (2002) 10503–10504, https://doi.org/10.1021/la0264623.

[11] K.J. Blackshaw, M.G. Varmecky, J.D. Patterson, Interfacial structure and partitioning of nitrate ions in reverse micelles, J. Phys. Chem. A 123 (2019) 336–342, https://doi.org/10.1021/acs.jpca.8b09751.

[12] M.R. Harpham, B.M. Ladanyi, N.E. Levinger, K.W. Herwig, Water motion in reverse micelles studied by quasielastic neutron scattering and molecular dynamics simulations, J. Chem. Phys. 121 (2004) 7855–7868, https://doi.org/10.1063/1.1792592.

[13] J. Eastoe, B.H. Robinson, R.K. Heenan, Water-in-oil microemulsions formed by ammonium and tetrapropylammonium salts of aerosol OT, 1993. https://pubs.acs.org/sharingguidelines.

[14] M. Bey Temsamani, M. Maeck, I. El Hassani, H.D. Hurwitz, Fourier transform infrared investigation of water states in aerosol-OT reverse micelles as a function of counterionic nature, J. Phys. Chem. B 102 (1998) 3335–3340, https://doi.org/10.1021/jp971844g.

[15] N.M. Correa, N.E. Levinger, What can you learn from a molecular probe? New insights on the behavior of C343 in homogeneous solutions and AOT reverse micelles, J. Phys. Chem. B 110 (2006) 13050–13061, https://doi.org/10.1021/jp0572636.

[16] E.M. Adams, H. Hao, I. Leven, M. Rüttermann, H. Wirtz, M. Havenith, T. Head-Gordon, Proton Traffic Jam: effect of nanoconfinement and acid concentration on proton hopping mechanism, Angew. Chem. Int. Ed. 60 (2021) 25419–25427, https://doi.org/10.1002/anie.202108766.

[17] J. Eastoe, M.J. Hollamby, L. Hudson, Recent advances in nanoparticle synthesis with reversed micelles, Adv. Colloid Interface Sci. 128–130 (2006) 5–15, https://doi.org/10.1016/J.CIS.2006.11.009.

[18] R.D. Falcone, N.M. Correa, J.J. Silber, On the formation of new reverse micelles: a comparative study of benzene/surfactants/ionic liquids systems using UV−visible absorption spectroscopy and dynamic light scattering, Langmuir 25 (2009) 10426–10429, https://doi.org/10.1021/la901498e.

[19] Y. Zheng, W. Eli, G. Li, FTIR study of Tween80/1-butyl-3-methylimidazolium hexafluorophosphate/toluene microemulsions, Colloid Polym. Sci. 287 (2009) 871–876, https://doi.org/10.1007/s00396-009-2044-x.

[20] N.K. Richards, L.M. Wingen, K.M. Callahan, N. Nishino, M.T. Kleinman, D. J. Tobias, B.J. Finlayson-Pitts, Nitrate ion photolysis in thin water films in the presence of bromide ions, J. Phys. Chem. A 115 (2011) 5810–5821, https://doi.org/10.1021/jp109560j.

[21] D.J. Tobias, J.C. Hemminger, Getting specific about specific ion effects, Science 319 (2008) 1197–1198, https://doi.org/10.1126/science.1152799, 1979.

[22] L.M. Wingen, A.C. Moskun, S.N. Johnson, J.L. Thomas, M. Roeselova, D.J. Tobias, M.T. Kleinman, B.J. Finlayson-Pitts, Enhanced surface photochemistry in chloride-nitrate ion mixtures, Phys. Chem. Chem. Phys. 10 (2008) 5668–5677, https://doi.org/10.1039/b806613b.

[23] M.A. Brown, B. Winter, M. Faubel, J.C. Hemminger, Spatial distribution of nitrate and nitrite anions at the liquid/vapor interface of aqueous solutions, J. Am. Chem. Soc. 131 (2009) 8354–8355, https://doi.org/10.1021/ja901791v.

[24] J. Cheng, C.D. Vecitis, M.R. Hoffmann, A.J. Colussi, Experimental anion affinities for the air/water interface, J. Phys. Chem. B 110 (2006) 25598–25602, https://doi.org/10.1021/jp066197k.

[25] L. Götte, K.M. Parry, W. Hua, D. Verreault, H.C. Allen, D.J. Tobias, Solvent-shared ion pairs at the air-solution interface of magnesium chloride and sulfate solutions revealed by sum frequency spectroscopy and molecular dynamics simulations, J. Phys. Chem. A 121 (2017) 6450–6459, https://doi.org/10.1021/acs.jpca.7b05600.

[26] J.D. Patterson, P.J. Reid, Time-resolved infrared absorption studies of the solvent-dependent photochemistry of ClNO, J. Phys. Chem. B 116 (2012) 10437–10443, https://doi.org/10.1021/jp211697r.

[27] P. Jungwirth, D.J. Tobias, Molecular structure of salt solutions: a new view of the interface with implications for heterogeneous atmospheric chemistry, J. Phys. Chem. B 105 (2001) 10468–10472, https://doi.org/10.1021/jp012750g.

[28] P. Jungwirth, D. J. Tobias, Ions at the air/water interface, J. Phys. Chem. B 106 (2002) 6361–6373, https://doi.org/10.1021/jp020242g.

[29] A.J. Bard, L.R. Faulkner, Electrochemical Methods: Fundamentals and Applications, Wiley, New York, 1980.

[30] W. Hua, D. Verreault, H.C. Allen, Relative order of sulfuric acid, bisulfate, hydronium, and cations at the air–water interface, J. Am. Chem. Soc. 137 (2015) 13920–13926, https://doi.org/10.1021/jacs.5b08636.

[31] A.P. Ault, T.L. Guasco, O.S. Ryder, J. Baltrusaitis, L.A. Cuadra-Rodriguez, D. B. Collins, M.J. Ruppel, T.H. Bertram, K.A. Prather, V.H. Grassian, Inside versus outside: ion redistribution in nitric acid reacted sea spray aerosol particles as

determined by single particle analysis, J. Am. Chem. Soc. 135 (2013) 14528–14531, https://doi.org/10.1021/ja407117x.

[32] A. Vila Verde, M. Santer, R. Lipowsky, Solvent-shared pairs of densely charged ions induce intense but short-range supra-additive slowdown of water rotation, Phys. Chem. Chem. Phys. 18 (2016) 1918–1930, https://doi.org/10.1039/C5CP05726D.

[33] N.H.C. Lewis, J.A. Fournier, W.B. Carpenter, A. Tokmakoff, Direct observation of ion pairing in aqueous nitric acid using 2D infrared spectroscopy, J. Phys. Chem. B 123 (2019) 225–238, https://doi.org/10.1021/acs.jpcb.8b10019.

[34] M. Crowder, F. Tahiry, I. Lizarraga, S. Rodriguez, N. Peña, A.K. Sharma, Computational analysis of water dynamics in AOT reverse micelles, J. Mol. Liq. 375 (2023), https://doi.org/10.1016/j.molliq.2023.121340.

[35] A.V. Martinez, L. Dominguez, E. Małolepsza, A. Moser, Z. Ziegler, J.E. Straub, Probing the structure and dynamics of confined water in AOT reverse micelles, J. Phys. Chem. B 117 (2013) 7345–7351, https://doi.org/10.1021/jp402270e.

[36] V.R. Hande, S. Chakrabarty, Exploration of the presence of bulk-like water in AOT reverse micelles and water-in-oil nanodroplets: the role of charged interfaces, confinement size and properties of water, Phys. Chem. Chem. Phys. 18 (2016) 21767–21779, https://doi.org/10.1039/C6CP04378J.

[37] B.K. Paul, D. Ray, N. Guchhait, Binding interaction and rotational-relaxation dynamics of a cancer cell photosensitizer with various micellar assemblies, J. Phys. Chem. B 116 (2012) 9704–9717, https://doi.org/10.1021/jp304280m.

[38] R. Sett, S. Sen, B.K. Paul, N. Guchhait, How does nanoconfinement within a reverse micelle influence the interaction of phenazinium-based photosensitizers with DNA? ACS Omega 3 (2018) 1374–1385, https://doi.org/10.1021/acsomega.7b01820.

[39] S. Abel, M. Waks, M. Marchi, Molecular dynamics simulations of cytochrome c unfolding in AOT reverse micelles: the first steps, Eur. Phys. J. E 32 (2010) 399–409, https://doi.org/10.1140/epje/i2010-10635-x.

[40] D. Brown, J.H.R. Clarke, Molecular dynamics simulation of a model reverse micelle, J. Phys. Chem. 92 (1988) 2881–2888, https://doi.org/10.1021/j100321a036.

[41] V.R. Vasquez, B.C. Williams, O.A. Graeve, Stability and comparative analysis of AOT/water/isooctane reverse micelle system using dynamic light scattering and molecular dynamics, J. Phys. Chem. B 115 (2011) 2979–2987, https://doi.org/10.1021/jp109202f.

[42] A. Gardner, V.R. Vásquez, A. Clifton, O.A. Graeve, Molecular dynamics analysis of the AOT/water/isooctane system: effect of simulation time, initial configuration, and model salts, Fluid Phase Equilib. 262 (2007) 264–270, https://doi.org/10.1016/J.FLUID.2007.09.013.

[43] S. Abel, F. Sterpone, S. Bandyopadhyay, M. Marchi, Molecular modeling and simulations of AOT–water reverse micelles in isooctane: structural and dynamic properties, J. Phys. Chem. B 108 (2004) 19458–19466, https://doi.org/10.1021/jp047138e.

[44] J. Chowdhary, B.M. Ladanyi, Molecular dynamics simulation of aerosol-OT reverse micelles, J. Phys. Chem. B 113 (2009) 15029–15039, https://doi.org/10.1021/jp906915q.

[45] M. Marchi, S. Abel, M. Massimo, A. Stephane, Modeling the self-aggregation of small AOT reverse micelles from first-principles, J. Phys. Chem. Lett. 6 (2015) 170–174, https://doi.org/10.1021/jz5023619.

[46] H.J.C. Berendsen, D. van der Spoel, R. van Drunen, GROMACS: a message-passing parallel molecular dynamics implementation, Comput. Phys. Commun. 91 (1995) 43–56, https://doi.org/10.1016/0010-4655(95)00042-E.

[47] S. Páll, M. Abraham, C. Kutzner, B. Hess, E. Lindahl, Tackling exascale software challenges in molecular dynamics simulations with GROMACS, in: S. Markidis, E. Laure (Eds.), Solving Software Challenges for Exascale, Springer International Publishing, 2015, pp. 3–27, https://doi.org/10.1007/978-3-319-15976-8_1.

[48] L. Martínez, R. Andrade, E.G. Birgin, J.M. Martínez, PACKMOL: a package for building initial configurations for molecular dynamics simulations, J. Comput. Chem. 30 (2009) 2157–2164, https://doi.org/10.1002/jcc.21224.

[49] H. Fathi, J.P. Kelly, V.R. Vasquez, O.A. Graeve, Ionic concentration effects on reverse micelle size and stability: implications for the synthesis of nanoparticles, Langmuir 28 (2012) 9267–9274, https://doi.org/10.1021/la300586f.

[50] K. Vanommeslaeghe, E. Hatcher, C. Acharya, S. Kundu, S. Zhong, J. Shim, E. Darian, O. Guvench, P. Lopes, I. Vorobyov, A.D. Mackerell, CHARMM general force field: a force field for drug-like molecules compatible with the CHARMM all-atom additive biological force fields, J. Comput. Chem. 31 (2009), https://doi.org/10.1002/jcc.21367. NA-NA.

[51] J. Chowdhary, B.M. Ladanyi, Molecular dynamics simulation of aerosol-OT reverse micelles, J. Phys. Chem. B 113 (2009) 15029–15039.

[52] A.V. Martinez, L. Dominguez, E. Malolepsza, A. Moser, Z. Ziegler, J.E. Straub, Probing the structure and dynamics of confined water in AOT reverse micelles, J. Phys. Chem. B 117 (2013) 7345–7351.

[53] W.L. Jorgensen, J. Chandrasekhar, J.D. Madura, R.W. Impey, M.L. Klein, Comparison of simple potential functions for simulating liquid water, J. Chem. Phys. 79 (1983) 926, https://doi.org/10.1063/1.445869.

[54] S. Strande, H. Cai, M. Tatineni, W. Pfeiffer, C. Irving, A. Majumdar, D. Mishin, R. S. Sinkovits, M.M. Norman, N. Wolter, T. Cooper, I. Altintas, M. Kandes, I. Perez, M. Shantharam, M. Thomas, S. Sivagnanam, T. Hutton, H. Cai, T. Cooper, C. Irving, T. Hutton, M. Kandes, A. Majumdar, D. Mishin, I. Perez, W. Pfeiffer, M. Shantharam, R.S. Sinkovits, S. Sivagnanam, S. Strande, M. Tatineni, M. Thomas, N. Wolter, M.M. Norman, T. Hut-Ton, Expanse: Computing without Boundaries: Architecture, Deployment, and Early Operations Experiences of a Supercomputer Designed For the Rapid Evolution in Science and Engineering, in: Practice and Experience in Advanced Research Computing, Association for Computing Machinery, New York, NY, USA, 2021, https://doi.org/10.1145/3437359.

[55] J. Towns, T. Cockerill, M. Dahan, I. Foster, K. Gaither, A. Grimshaw, V. Hazlewood, S. Lathrop, D. Lifka, G.D. Peterson, R. Roskies, J.R. Scott, N. Wilkins-Diehr, XSEDE: accelerating scientific discovery, Comput. Sci. Eng. 16 (2014) 62–74, https://doi.org/10.1109/MCSE.2014.80.

[56] U. Essmann, L. Perera, M.L. Berkowitz, T. Darden, H. Lee, L.G. Pedersen, A smooth particle mesh Ewald method, J. Chem. Phys. 103 (1995) 8577–8593, https://doi.org/10.1063/1.470117.

[57] P. Mukherjee, S. Gupta, S. Rafiq, R. Yadav, V.K. Jain, J. Raval, P. Sen, Ramping of pH across the water-pool of a reverse micelle, Langmuir 32 (2016) 1693–1699, https://doi.org/10.1021/acs.langmuir.5b04429.

[58] M.S. Bakshi, How surfactants control crystal growth of nanomaterials, Cryst. Growth Des. 16 (2016) 1104–1133, https://doi.org/10.1021/acs.cgd.5b01465.

[59] M.V. Kovalenko, M.I. Bodnarchuk, R.T. Lechner, G. Hesser, and F. Schäffler, W. Heiss, Fatty acid salts as stabilizers in size- and shape-controlled nanocrystal synthesis: the case of inverse spinel iron oxide, (2007). 10.1021/JA0692478.

[60] M.P. Pileni, The role of soft colloidal templates in controlling the size and shape of inorganic nanocrystals, Nat. Mater. 2 (2003) 145–150, https://doi.org/10.1038/nmat817.

[61] M.R. Harpham, B.M. Ladanyi, N.E. Levinger, The effect of the counterion on water mobility in reverse micelles studied by molecular dynamics simulations, J. Phys. Chem. B 109 (2005) 16891–16900, https://doi.org/10.1021/jp0527731.

[62] J. Faeder, B.M. Ladanyi, Molecular dynamics simulations of the interior of aqueous reverse micelles, J. Phys. Chem. B 104 (2000) 1033–1046, https://doi.org/10.1021/jp993076u.

[63] I.R. Piletic, D.E. Moilanen, D.B. Spry, N.E. Levinger, M.D. Fayer, Testing the core/shell model of nanoconfined water in reverse micelles using linear and nonlinear IR spectroscopy, J. Phys. Chem. A 110 (2006) 4985–4999, https://doi.org/10.1021/jp061065c.

[64] S. Park, D.E. Moilanen, M.D. Fayer, Water dynamics-The effects of ions and nanoconfinement, J. Phys. Chem. B 112 (2008) 5279–5290, https://doi.org/10.1021/jp7121856.

[65] M.D. Fayer, Dynamics of water interacting with interfaces, molecules, and ions, Acc. Chem. Res. 45 (2012) 3–14, https://doi.org/10.1021/ar2000088.

[66] D.E. Moilanen, N.E. Levinger, D.B. Spry, M.D. Fayer, Confinement or the nature of the interface? Dynamics of nanoscopic water, J. Am. Chem. Soc. 129 (2007) 14311–14318, https://doi.org/10.1021/ja073977d.

[67] P. Jungwirth, B.J. Finlayson-Pitts, D.J. Tobias, Introduction: structure and chemistry at aqueous interfaces, Chem. Rev. 106 (2006) 1137–1139, https://doi.org/10.1021/cr040382h.

[68] P.K. Singh, D.G. Kuroda, R.M. Hochstrasser, An Ion's perspective on the molecular motions of nanoconfined water: a two-dimensional infrared spectroscopy study, J. Phys. Chem. B 117 (2013) 9775–9784, https://doi.org/10.1021/JP406725A.

[69] A.K. Mora, P.K. Singh, S.A. Nadkarni, S. Nath, How mobile is the water in the reverse micelles? A 2DIR study with an ultrasmall IR probe, J. Mol. Liq. 327 (2021), 114819, https://doi.org/10.1016/J.MOLLIQ.2020.114819.